nature communications

Article

https://doi.org/10.1038/s41467-025-67548-0

Intervention timing and disease stage shape tecovirimat and cidofovir efficacy in male SCID mice

Received: 19 April 2025

Accepted: 3 December 2025

Published online: 18 December 2025

Check for updates

Xinyu Cao[1,2,6], Ning Shi[3,6], Xiangshu Qiu[2,4], Jiaxin Tian[2,4], Peng Wang[2,4], Bocheng Liu[2], Zhuo Ha[2], He Zhang[2], Chao Shang[2], Xiao Li[2], Yubiao Xie[2,7] ✉, Yuelong Shu[1,7] ✉ & Huijun Lu[2,5,7] ✉

Currently, mpox virus (MPXV) continues to pose a global public health challenge, with immunocompromised individuals often exhibiting more severe clinical symptoms. This study screens three male mouse models (ICR, IFNAR1$^{-/-}$, SCID) and identifies SCID mice as the optimal model for modeling severe patient symptoms, including pneumonia, rash, and localized inflammation, which is applied to evaluate the antiviral efficacy of tecovirimat and cidofovir. Both drugs prevent systemic MPXV spread when administered within two days post virus exposure. Local antiviral efficacy differs between the two drugs, particularly after intradermal infection. Prolonged treatment up to 28 days post infection results in 100% survival of SCID mice but fails to effectively suppress localized rash and inflammatory swelling, suggesting that the drugs have limited impact at later stages of the disease. These findings indicate that the therapeutic efficacy of tecovirimat and cidofovir depends on the timing of intervention initiation and the stage of disease progression.

As a significant member of the genus *Orthopoxvirus* from the family *Poxviridae*[1], mpox virus (MPXV) is taxonomically related to variola virus (smallpox virus). While smallpox virus demonstrates significantly higher human transmissibility and lethality compared to MPXV, accumulating epidemiological data suggest that MPXV is undergoing microevolution[2,3]. Phylogenetic studies classify MPXV into four clades, including Ia, Ib, IIa, and IIb[4]. Clade IIb has circulated among humans since 2016, leading to the 2022 pandemic[5,6].

Regarding clinical manifestations, the MPXV clade IIb predominantly affects men who have sex with men (MSM), accounting for 87% of the reported cases, of whom approximately 50% are HIV-positive. These patients with co-infection, particularly those with advanced HIV, exhibit severe complications and suffer from an increased risk of mortality[7]. Among patients with MPXV and HIV co-infection, 29% develop pulmonary involvement[8]. The first documented case of MPXV-induced pneumonia was observed in a male patient with advanced AIDS who presented with several complications and finally succumbed to sepsis[9]. Cutaneous rash occurs in 95% of MPXV-infected patients[10]. The rash is typically self-limiting in immunocompetent individuals, spontaneously resolving within 2–4 weeks[10]. However, immunocompromised patients often develop more extensive and persistent skin lesions, have higher viral loads, suffer from prolonged disease, and are at a significantly increased risk of scarring[11]. Additionally, separate studies have reported that myalgia (31%) and

[1]Key Laboratory of Pathogen Infection Prevention and Control (MOE), State Key Laboratory of Respiratory Health and Multimorbidity, National Institute of Pathogen Biology, Chinese Academy of Medical Sciences & Peking Union Medical College, Beijing 102629, China. [2]Changchun Veterinary Research Institute, Chinese Academy of Agricultural Sciences, Changchun 130122, China. [3]State Key Laboratory for Diagnosis and Treatment of Severe Zoonotic Infectious Diseases, Key Laboratory for Zoonosis Research of the Ministry of Education, Institute of Zoonosis, and College of Veterinary Medicine, Jilin University, Changchun 130062, China. [4]College of Animal Sciences, Institute of Preventive Veterinary Medicine, Zhejiang University, Hangzhou, Zhejiang 310063, China. [5]Research Unit of Key Technologies for Prevention and Control of Virus Zoonoses, Chinese Academy of Medical Sciences, Changchun 130122, China. [6]These authors contributed equally: Xinyu Cao, Ning Shi. [7]These authors jointly supervised this work: Yubiao Xie, Yuelong Shu, Huijun Lu ✉e-mail: 877216599@163.com; yshu@ipbcams.ac.cn; huijun_lu@126.com

localized joint swelling (rarely) as a localized symptom[10,12–14]. Currently, there is a lack of studies on systematically establishing animal models that simulate mpox virus infection in immunocompromised populations based on multiple clinical symptoms.

In light of the severe manifestations in high-risk groups, the search for effective therapeutics becomes critical. To date, no antiviral treatment has been definitively demonstrated to be effective against MPXV. However, several antiviral agents have been authorized for emergency use in certain countries and are under evaluation in clinical trials. WHO and several national guidelines recommended tecovirimat as the first-line antiviral drug for mpox, showing efficacy in several clinical cases[15–17]. However, recent studies reported that, during the mpox outbreak in the United States, severely immunocompromised patients who received multiple courses of tecovirimat exhibited poor outcomes (35.3%; 18 out of 51 patients)[18,19]. Furthermore, tecovirimat resistance is a major clinical challenge, particularly in subjects with severe immune dysfunction. Resistance-associated mutations, such as F13L gene mutation, may lead to treatment failure and human-to-human transmission, emphasizing the need for cautious use of tecovirimat until obtaining more experimental data[20–22]. Cidofovir exhibits broad-spectrum activity against DNA viruses, such as MPXV. A patient with HIV and uncontrolled viremia exhibited marked improvement after switching to cidofovir after failure of treatment with tecovirimat and antibiotics[23]. However, cidofovir exhibits nephrotoxicity, particularly in patients with HIV, with an incidence rate of nearly 25%[24]. Additionally, the topical application of cidofovir may lead to adverse effects, such as skin erosions[25]. Due to the risk of such adverse events, cidofovir is often reserved for critical cases or tecovirimat-resistant infections; therefore, there are limited experimental data on its monotherapy.

In this work, we systematically establish pneumonia, cutaneous lesion, and localized inflammation models in SCID mice infected with MPXV clade IIb. All three models recapitulate key clinical manifestations observed in high-risk populations, including people living with HIV and organ transplant recipients, with systemic viral dissemination to internal organs also being demonstrated. In all short-term infection models, treatment with either tecovirimat or cidofovir initiated within two days post-exposure significantly reduced viral loads in susceptible organs and effectively suppressed clinical symptoms, including rash and localized inflammatory swelling. In late-stage infection models, both drugs suppress systemic MPXV dissemination and ensure the survival of all models, but fail to alleviate local clinical symptoms in the skin and footpads of the lesion and localized inflammation models.

Results

Screening and establishment of the mouse model of MPXV clade IIb-induced pneumonia

Intranasal (I.N.) inoculation is commonly employed for modeling pneumonia in small rodents, but the pathogenicity of MPXV clade IIb varies across different mouse models. In this study, male ICR mice, IFNAR1$^{-/-}$ mice, and SCID mice were intranasally inoculated with 10^5 PFU MPXV clade IIb or sterile saline (control group). After MPXV clade IIb infection, ICR and IFNAR1$^{-/-}$ mice exhibited a steady increase in body weight, which was comparable to the control group. SCID mice exhibited a significant decrease in body weight at 12 days post infection (dpi), which was recovered by 14 dpi (Fig. 1a). After inoculation, no clinical symptoms, such as changes in behavior, appetite, fur, or appearance, were observed in any of the three mouse models. Gross examination of lung tissues collected at 3 dpi, 7 dpi, and 14 dpi exhibited no significant differences compared to the control group, except for mild hemorrhage and atrophy in the lung tissue of SCID mice at 14 dpi (Fig. 1b). Additionally, qPCR and detection of virus titer were conducted to measure the viral DNA loads and infectious virus titers in the lung, liver and spleen of the three mouse models at 3 dpi, 7 dpi, and 14 dpi. The results indicated that ICR mice were not susceptible to MPXV clade IIb. Viral DNA and virus titer in the lung were at low levels at 3 dpi, decreasing to the detection limit at 7 dpi and 14 dpi. In addition, viral DNA levels and infectious titers in liver and spleen tissues remained below the detection limit throughout the entire observation period (Fig. 1c, d). IFNAR1$^{-/-}$ mice exhibited peak lung infection on 7 dpi, with a median viral DNA load of $10^{4.48}$ copies/mL, and a low median virus titer of $10^{2.43}$ $TCID_{50}$/mL (Fig. 1c, d). While both viral loads and virus titers in the spleen and liver remained below the detection limit throughout the study (Fig. 1e–h). After intranasal inoculation, mice with SCID revealed a steady increase in lung viral load and virus titer over time. This model exhibited the greatest increase in virus titer compared to the other two mouse models, with the lung viral load reaching a median of $10^{4.75}$ $TCID_{50}$/mL at 14 dpi (Fig. 1c, d). Viral loads and infectious titers in the spleen and liver began to be detected after 7 dpi (Fig. 1e–h). These findings suggest that SCID mice are the most stable and susceptible model for the intranasal infection study.

Subsequently, SCID mice were intranasally inoculated with MPXV clade IIb at the same virus titer (n = 8), and their clinical disease scores and survival rates were monitored for up to 28 dpi to observe the typical clinical symptoms. From 16 dpi, weight loss, lethargy, dishevelled fur, swollen footpads, and the typical symptoms of MPXV clade IIb infection, such as skin lesions of the tail were observed in SCID mice (Supplementary Fig. 1) The median disease score of 7 at 28 dpi (Fig. 1i, Supplementary Fig. 2a), according to Supplementary Table 1, with a relatively low mortality rate of 25% (Fig. 1j). Additionally, the cytokine detection showed significantly higher mRNA levels of pro-inflammatory factors (*TNF-α* and *IL-6*) and antiviral interferons (*IFN-β* and *IFN-α1*), while the mRNA levels of *NAP3* were significantly down-regulated (Supplementary Fig. 3a). Notably, compared to other mouse models of intranasal infection, footpad edema and cutaneous lesions were observed in this study. These symptoms indicate that intranasal MPXV clade IIb infection in SCID mice can induce viremia during the late stage of infection.

In summary, among the three murine models evaluated (ICR, IFNAR1$^{-/-}$ and SCID), SCID mice emerged as the most sensitive to MPXV clade IIb infection. It shows progressive weight loss and systemic multi-organ infection in the early stage of infection, and skin lesions, footpad swelling, and even partial death are observed in the late stage, which is suitable for the evaluation research of antiviral drugs.

Screening and establishment of the mouse model of MPXV clade IIb-induced skin lesion

Skin scratches were created in the tails to simulate the MPXV-associated cutaneous rash. Male ICR, IFNAR1$^{-/-}$, and SCID mice were intradermally inoculated with 10^5 PFU MPXV clade IIb or sterile saline (control group). After virus inoculation, the body weights of ICR and IFNAR1$^{-/-}$ mice increased steadily, with no significant difference between the model group and the control group. SCID mice exhibited a significant decrease in body weight from 10 dpi (Fig. 2a). All three models exhibited certain scabs (width ≥1 mm), with ICR mice exhibiting the lowest probability of forming infectious scabs and recovery by 7 dpi. IFNAR1$^{-/-}$ mice had the highest scab formation rate at 7–9 dpi, reaching 75% and beginning to recover from 10 dpi. SCID mice exhibited the highest scab formation rate at 6 dpi, reaching 100%, and the symptoms worsened over time (Fig. 2b, c). Additionally, we measured viral DNA load and virus titer in the skin (Fig. 2d, e), lung (Fig. 2f, g), liver (Fig. 2h, i), and spleen (Fig. 2j, k) of the three mouse models at 3 dpi, 7 dpi, and 14 dpi using qPCR and virus titer detection. We found that the virus titer in ICR mice skin tissue remained around the detection limit, with viral DNA detectable only at 3 dpi and 7 dpi (Fig. 2d, e). The viral loads and virus titers in the lung, liver, and spleen were undetectable (Fig. 2f–k). IFNAR1$^{-/-}$ mice were more sensitive to MPXV clade IIb. Viral load and infectious titer were detectable in the skin between 3 and 14 dpi (Fig. 2d, e). In contrast, in the lung and liver,

https://doi.org/10.1038/s41467-025-67548-0

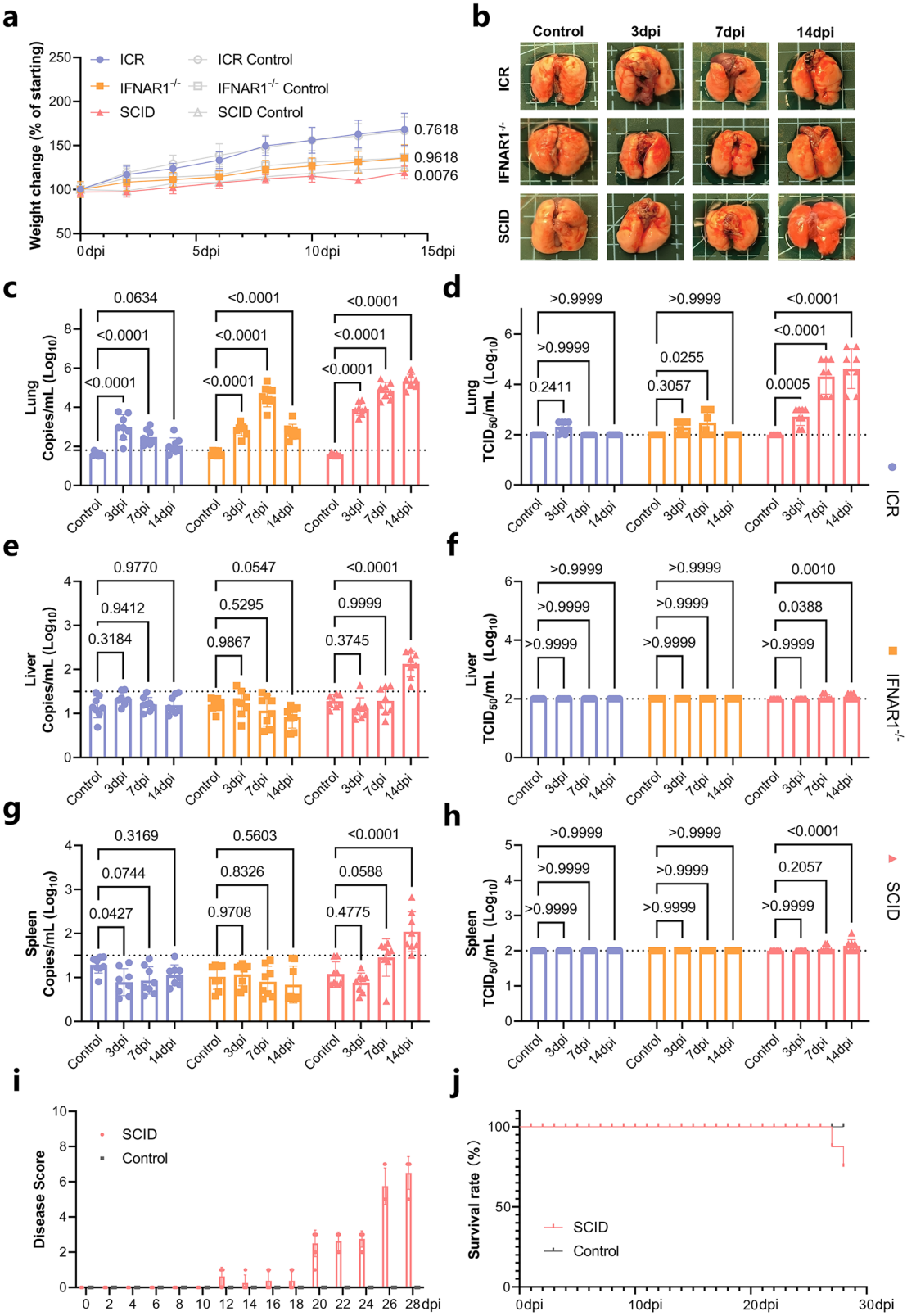

Fig. 1 | Phenotypic and viral dynamics analysis after intranasal infection of MPXV clade IIb in different mouse models. ICR (blue), IFNAR1$^{-/-}$ (yellow), and SCID (red) mice were intranasally inoculated with MPXV (10^5 PFU/100 µL, n = 24) or sterile saline (control group, n = 8). **a** The body weight changes were monitored from 0 to 14 dpi. **b** Pulmonary tissue appearance, viral DNA load (qPCR), and infectious viral titer ($TCID_{50}$) in the lung (**c**, **d**), liver (**e**, **f**), and spleen (**g**, **h**) were recorded at 3 dpi, 7 dpi, and 14 dpi. After identifying the most susceptible mice, SCID mice were inoculated with MPXV (red, 10^5 PFU/100 µL, n = 8) or sterile saline (gray, 100 µL, n = 8) via intranasal inoculation. **i** Disease score and **j** survival rate of SCID mice were monitored from 0 to 28 dpi. Dashed line: limit of blank. Error bars represent mean ± standard error of the mean (SEM). Statistical analysis in (**a**) was determined by *t*-tests, and in (**c**–**g**) was determined by one-way analysis of variance (ANOVA) followed by two-tailed *t*-tests. *P* values indicating statistical significance are displayed on the panels. Source data are provided as a Source data file.

https://doi.org/10.1038/s41467-025-67548-0

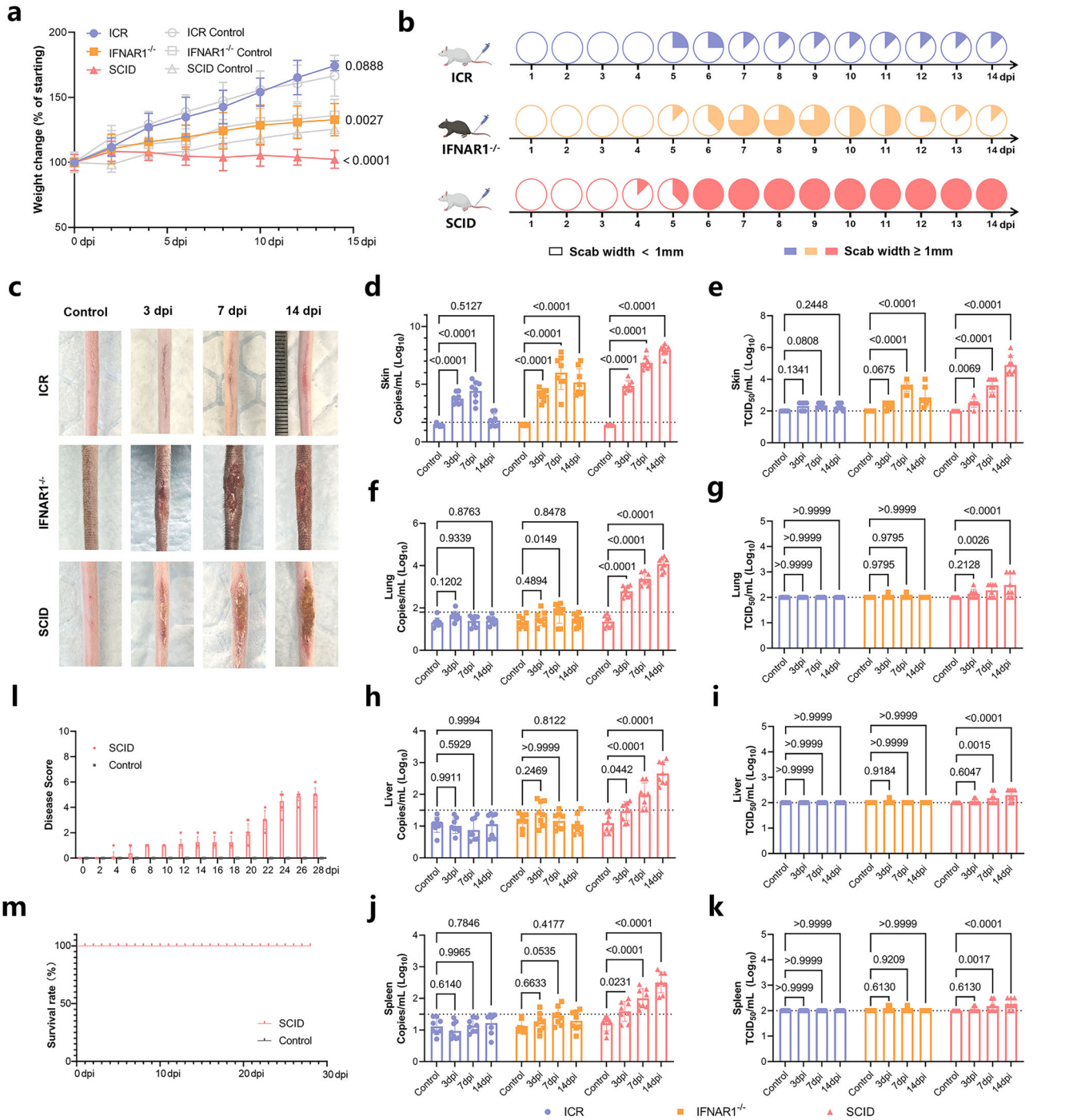

Fig. 2 | Phenotypic and viral dynamics analysis after intradermal infection of MPXV clade IIb in different mouse models. ICR (blue), IFNAR1$^{-/-}$ (yellow), and SCID (red) mice were intradermally inoculated with MPXV (10^5 PFU/100 µL, n = 8) or sterile saline (control group, n = 8). **a** Body weight changes (0–14 dpi). **b** Cumulative incidence rate (0–14 dpi). The scab width of ≥1 mm was considered positive (blue, yellow, red), while <1 mm was considered negative (white). **c** The typical scabs at the tail of ICR, IFNAR1$^{-/-}$, and SCID. Viral load (qPCR) and viral titer ($TCID_{50}$) in the skin (**d**, **e**), lung (**f**, **g**), liver (**h**, **i**), and spleen (**j**, **k**) at 3, 7, and 14 dpi. After identifying the most susceptible mice, SCID mice were inoculated with MPXV (red, 10^5 PFU/100 µL, n = 8) or sterile saline (gray, 100 µL, n = 8) via intradermal inoculation. **l** Disease scores and **m** survival rates of SCID mice (0–28 dpi). Dashed line: limit of blank. Error bars represent the mean ± standard error of the mean (SEM). Statistical analysis in (**a**) was determined by *t*-tests, and in (**d**–**k**) was determined by one-way analysis of variance (ANOVA) followed by two-tailed *t*-tests. *P* values indicating statistical significance are displayed on the panels. Source data are provided as a Source data file. **b** was created with MedPeer (medpeer.cn).

viral loads above the detection limit were only observed at 3 and 7 dpi, while infectious virus titers were detected near the limit of detection at these time points. The virus titers of lung, liver, and spleen were decreased at 14 dpi, similar to the intranasal infection model (Fig. 2f–k). Consistent with the clinical manifestations, SCID mice exhibited the highest viral loads and virus titers in skin, lung, liver, and spleen among the three models. Viral loads were detectable as early as 3 dpi and increased steadily. However, infectious viral particles in lung, liver, and spleen were first detected from 7 dpi (Fig. 2d–k).

The most susceptible SCID mice were intradermally inoculated at the same virus titer for long-term observation up to 28 dpi. At 20 dpi, clinical symptoms, such as lethargy, disheveled fur, and rashes in non-

https://doi.org/10.1038/s41467-025-67548-0

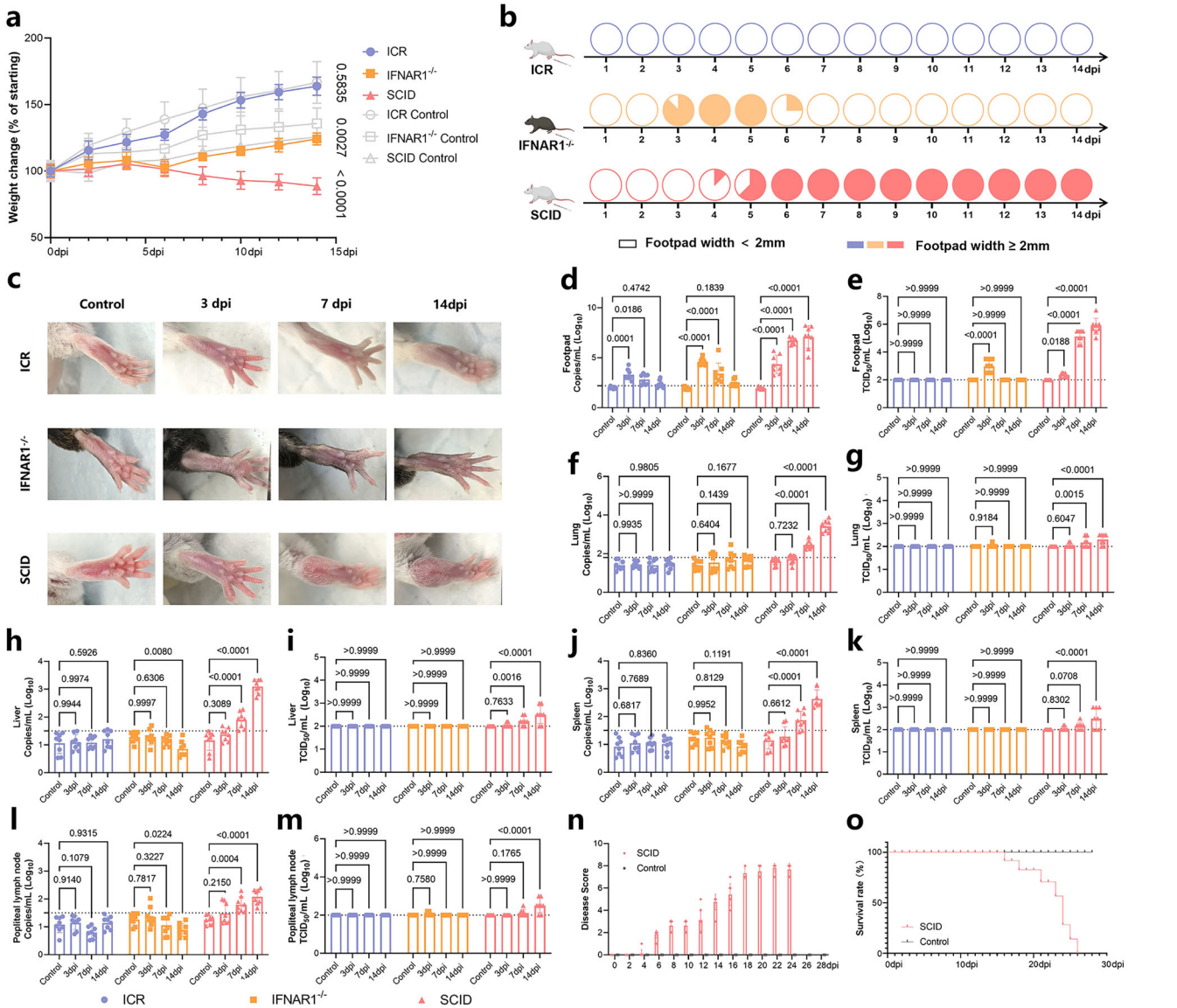

Fig. 3 | Phenotypic and viral dynamics analysis after subcutaneous infection of MPXV clade IIb in different mouse models. ICR (blue), IFNAR1$^{-/-}$ (yellow), and SCID (red) mice were subcutaneously inoculated in the footpad with MPXV (10^5 PFU/100 μL, n = 8) or sterile saline (control group, n = 8). **a** Body weight changes (0–14 dpi). **b** Cumulative incidence rate (0–14 dpi). The footpad width of ≥2 mm was considered positive (blue, yellow, red), while <2 mm was considered negative (white). **c** The typical swelling at the footpad. Viral load (qPCR) and viral titer ($TCID_{50}$) in footpad (**d**, **e**), lung (**f**, **g**), liver (**h**, **i**), spleen (**j**, **k**), and popliteal lymph nodes (**l**, **m**) at 3, 7, and 14 dpi. After identifying the most susceptible mice, SCID mice were inoculated with MPXV (red, 10^5 PFU/100 μL, n = 8) or sterile saline (gray, 100 μL, n = 8) via subcutaneous inoculation. **n** Disease scores and **o** survival rates of SCID mice (0–28 dpi). Dashed line: limit of blank. Error bars represent the mean ± standard error of the mean (SEM). Statistical analysis in (**a**) was determined by *t*-tests, and in (**d**–**m**) was determined by one-way analysis of variance (ANOVA) followed by two-tailed *t*-tests. *P* values indicating statistical significance are displayed on the panels. Source data are provided as a Source data file. **b** was created with MedPeer (medpeer.cn).

lesional areas, were observed in SCID mice. The disease score at the end of the infectious period was 5 (Fig. 2l, Supplementary Fig. 2b), with no deaths occurred (Fig. 2m). The changes in the levels of pro-inflammatory factors (*TNF-α* and *IL-6*), chemokines *NAP3* and antiviral interferons (*IFN-β* and *IFN-α1*) in the skin were consistent with those observed in the pneumonia model, with a further increase in *GM-CSF* levels (Supplementary Fig. 3b).

In summary, SCID mice demonstrated highest susceptibility to MPXV clade IIb following intradermal infection, exhibiting weight loss and characteristic crusted lesions. Although no mortality was observed, persistent skin rash and systemic dissemination to the lungs, liver, and spleen were documented, with viral loads in these organs showing a time-dependent increase.

Screening and establishment of the mouse model of MPXV clade IIb-induced local inflammation

Male ICR, IFNAR1$^{-/-}$, and SCID mice were subcutaneously inoculated at footpads with 10^5 PFU MPXV clade IIb or sterile saline (control group). Following viral inoculation, the increase in the body weight of ICR mice was comparable to that of the control group. IFNAR1$^{-/-}$ mice exhibited a significant decrease in body weight from 6 dpi, which normalized at 14 dpi. In contrast, SCID mice began to show a sustained decrease in body weight from 8 dpi (Fig. 3a). Between 0 and 14 dpi, only ICR mice did not exhibit footpad swelling (width ≥2 mm). IFNAR1$^{-/-}$ mice developed footpad swelling from 3 dpi, which resolved within three days. SCID mice gradually developed footpad swelling since 4 dpi. The incidence of footpad swelling reached 100% by 6 dpi, with the swelling

https://doi.org/10.1038/s41467-025-67548-0

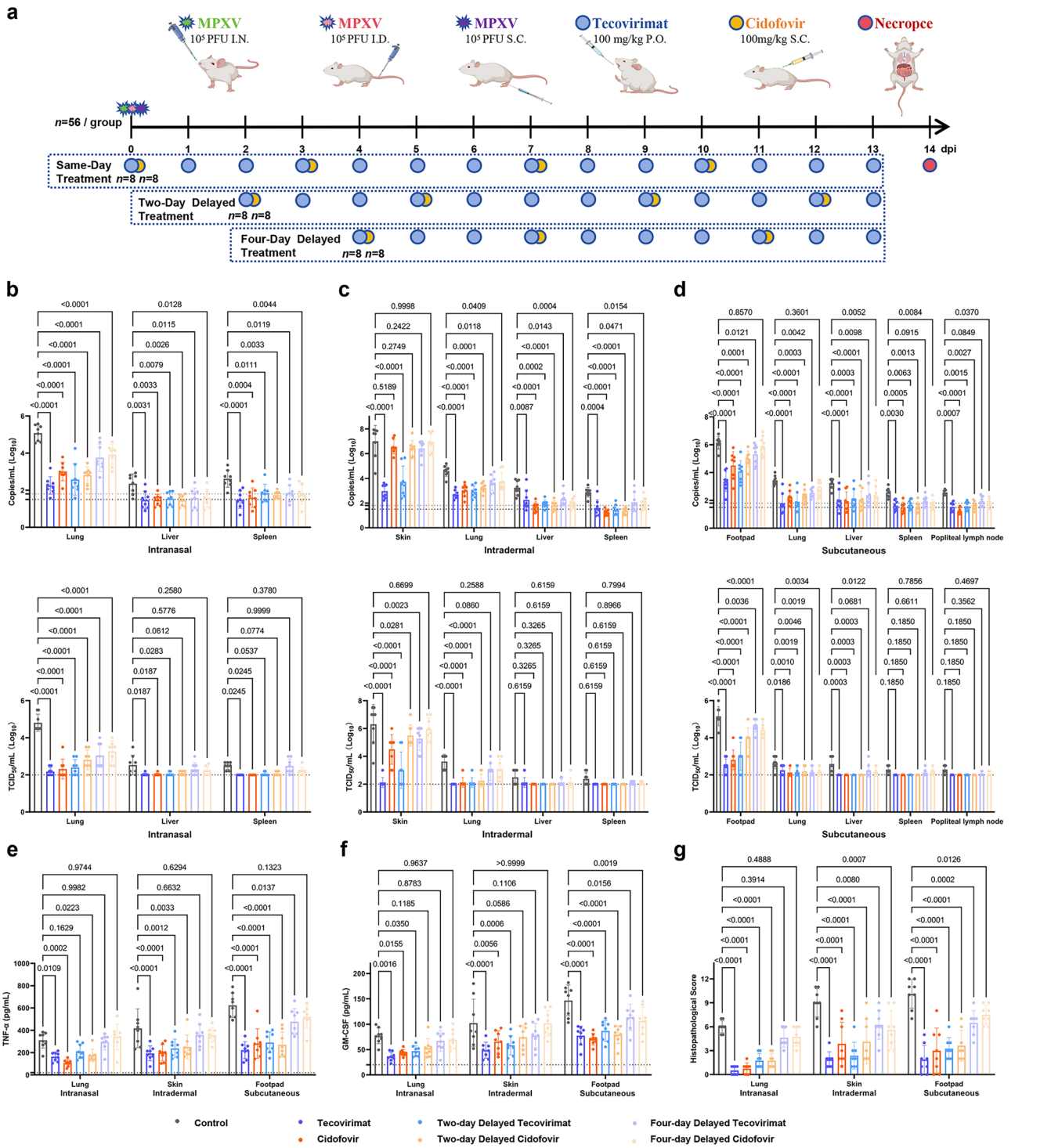

Fig. 4 | Time-dependent efficacy of tecovirimat and cidofovir against MPXV infection across multiple routes in SCID mice. a Study schematic of in vivo evaluation of tecovirimat and cidofovir was evaluated using SCID mice with intranasal (green asterisk, n = 56), intradermal (pink asterisk, n = 56), and subcutaneous (purple asterisk, n = 56) infection routes were shown. In each of the three infection models, animals were treated with either tecovirimat (blue circle, P.O., n = 8) or cidofovir (yellow circle, S.C., n = 8) at 2 h (designated as same day post-MPXV), 2 days, or 4 days post-MPXV exposure. Control groups received sterile saline via the corresponding routes (P.O., n = 4; S.C., n = 4). Mice were euthanized (red) at 14 dpi, and collect lungs, skin, footpad, liver, spleen, and popliteal lymph nodes. Viral load and titer in three infection models: **b** intranasal, **c** intradermal, and **d** subcutaneous. Cytokine expression levels of **e** TNF-α and **f** GM-CSF in lung, skin, and footpad tissues. **g** Histopathological damage scores of the tissues were evaluated by a certified, double-blind pathologist. Dashed line: limit of blank. Error bars represent the mean ± standard error of the mean (SEM). Statistical analysis was determined by one-way analysis of variance (ANOVA) followed by two-tailed *t*-tests. *P* values indicating statistical significance are displayed on the panels. Source data are provided as a Source data file. **a** was created with MedPeer (medpeer.cn).

progressively worsening thereafter. (Fig. 3b, c). Consistent with clinical observations, the virus titer in the footpad of ICR mice remained near the detection limit, with only trace amounts of viral DNA detected at 3 dpi and 7 dpi. IFNAR1$^{-/-}$ mice revealed moderate sensitivity to MPXV clade IIb, with detectable viral loads and titer observed only at 3 dpi and 7 dpi. SCID mice exhibited a continuous increase in both viral load and titer in the footpad throughout the disease course (Fig. 3d, e). The viral loads and titers in the lung, liver, spleen, and popliteal lymph nodes of ICR and IFNAR1$^{-/-}$ mice showed no significant differences compared to the 0 dpi control group. In contrast, the lung, liver, spleen, and popliteal lymph nodes of SCID mice exhibited a significant increase starting at 7 dpi (Fig. 3f–m). Both clinical symptoms and virus titer indicated that SCID mice were more susceptible to MPXV clade IIb.

We also monitored the clinical disease scores and survival rates of SCID mice up to 28 dpi using the same infection route and virus titer. SCID mice exhibited progressive footpad swelling, weight loss, lethargy, ruffled fur and skin papules (Supplementary Fig. 1). The clinical symptom score peaked at the end of the infectious period reaching a score of 8 (Fig. 3n, Supplementary Fig. 2c), with a 100% mortality rate at 25 dpi (Fig. 3o). The cytokine profiles in the footpad were generally consistent with those observed in the pneumonia model, although no increase was detected in *IFN-α1* levels (Supplementary Fig. 3c).

In summary, SCID mice exhibit maximum susceptibility to MPXV clade IIb following subcutaneous infection. This model initially develops localized swelling by day 4, progressing to systemic infection involving lungs, liver, spleen, and popliteal lymph nodes, accompanied by secondary rash. The disease progression culminates in 100% mortality during late stages.

Validation of tecovirimat and cidofovir in in vitro models

Tecovirimat and cidofovir have demonstrated antiviral activity against MPXV clade IIb in both clinical and preclinical studies. However, recent genomic alterations in the currently circulating clade IIb strains observed over the past 2 years may affect their susceptibility to these drugs. Therefore, the antiviral activity of tecovirimat and cidofovir against MPXV clade IIb was investigated. Based on the three disease models established previously, A549, HaCaT, LHCN-M2, and MC3T3 cell lines corresponding to the infected tissues were selected with the commonly used Vero-E6 cells. These in vitro models were employed to measure the drug concentrations with 50% cytotoxicity and 50% viral inhibition (CC_{50}, EC_{50}). The MC3T3 cell line, not previously reported in studies on MPXV, was confirmed to be susceptible to the MPXV clade IIb strain. The CC_{50} values for both tecovirimat and cidofovir were more than 200 μM in all four cell lines, suggesting low cytotoxicity. The EC_{50} values for tecovirimat against MPXV clade IIb ranged from 0.0029 to 0.01206 μM, which were lower than those for cidofovir (0.4414–2.931 μM) (Supplementary Fig. 4). These results are consistent with recent findings on other clade IIb isolates[26,27]. Overall, tecovirimat and cidofovir demonstrated potent inhibitory activity against MPXV clade IIb in several in vitro models.

Early administration of tecovirimat or cidofovir following MPXV clade IIb exposure significantly enhances treatment efficacy

Given the broad and potent in vitro inhibitory effects of tecovirimat and cidofovir on MPXV clade IIb, their in vivo efficacy was investigated using the three animal models established in this study. The SCID intranasal, intradermal, and subcutaneous infection models were employed in this study (Fig. 4a). In each of the three infection models, animals were treated with either tecovirimat (P.O., n = 8) or cidofovir (S.C., n = 8) at 2 h, 2 days, or 4 days post-MPXV clade IIb exposure. Control groups received sterile saline via the corresponding routes (P.O., n = 4; S.C., n = 4).

In the intranasal infection model, both tecovirimat and cidofovir significantly reduced viral loads in the lung, liver, and spleen when administered on the day of infection, or after a 2- or 4-day delay. However, no significant difference in viral titers was observed in the liver and spleen between the 2-day and 4-day delayed-treatment groups (Fig. 4b). In the intradermal infection model, tecovirimat significantly reduced viral load in the skin following both same-day and 2-day delayed treatment; the effect of cidofovir did not reach statistical significance. Conversely, both agents significantly reduced viral loads in the lung, liver, and spleen across all treatment timelines (same-day, 2-day, and 4-day delay). Notably, in the 4-day delayed-treatment group, only tecovirimat significantly suppressed viral titers in the skin and lung, with no statistically significant reduction observed in other organs (Fig. 4c). In the subcutaneous infection model, same-day and 2-day delayed administration of either drug significantly reduced viral loads in the footpad, lung, liver, spleen, and popliteal lymph nodes. Furthermore, both tecovirimat and cidofovir significantly decreased viral titers in the footpad and lung across all treatment schedules, including the 4-day delay group. Importantly, all treatment groups except the 4-day delay cohort achieved viral titers suppression below the limit of detection in the liver, spleen, and popliteal lymph nodes (Fig. 4d). In the target tissues of the three infection models, the inhibitory effects of tecovirimat and cidofovir on TNF-α and GM-CSF were time-dependent; specifically, the four-day delayed treatment lost such inhibitory effects in the pneumonia model and the rash model. (Fig. 4e, f).

Necropsy of the intranasally challenged group revealed pulmonary atrophy and hemorrhage. Histological examination by hematoxylin and eosin (H&E) staining further demonstrated severe pulmonary pathology, including alveolar wall thickening, alveolar collapse, inflammatory cell infiltration, hemorrhage, and epithelial cell necrosis (Fig. 5), with a median pathological score of 6 (Fig. 4g; Supplementary Table 1). In contrast, both tecovirimat and cidofovir treatment,whether administered on the day of challenge or after a two-day delay,resulted in only mild pathological changes; notably, lesions were more pronounced in the delayed-treatment group. Nevertheless, both regimens led to pathological scores significantly lower than those of the infected control (Fig. 4g). In the intradermally challenged group, skin tissues exhibited prominent scab formation. H&E analysis identified severe pathology characterized by fibrosis, inflammatory cell infiltration, cellular necrosis, acanthosis, keratinocyte ballooning degeneration, and crusting lesions (Fig. 5), yielding a median pathological score of 9 (Fig. 4g; Supplementary Table 2). Compared with the control group, both drug treatments resulted in significant histological improvement (Fig. 4g). Subcutaneous challenge induced severe localized swelling in footpad tissues. Pathological assessment revealed fibroplasia, inflammatory cell infiltration, chondrocyte necrosis, cartilage destruction, and pannus formation (Fig. 5), with a median score of 10 (Fig. 4g; Supplementary Table 3). Conversely, treated animals with mild ankle swelling displayed only fibrosis and inflammatory cell infiltration, while those without swelling showed no pathological damage (Fig. 5).

Collectively, based on an integrated assessment of viral load, infectious viral titer, cytokine levels, and histopathological damage, both tecovirimat and cidofovir demonstrated superior protective efficacy when administered on the day of exposure or after a two-day delay during the early stages of pneumonia, skin lesion formation, and localized footpad swelling. In contrast, therapeutic effectiveness was compromised in the four-day delayed-treatment group. This finding defined the optimal therapeutic window for tecovirimat and cidofovir in the SCID mouse model.

In late-stage SCID models of clade IIb MPXV infection, tecovirimat and cidofovir suppress systemic viral dissemination but fail to control the local rash and inflammation induced by MPXV

Although the recommended treatment duration for tecovirimat and cidofovir is 14 days, clinical practice often considers appropriately extending the treatment period for immunodeficient patients with

https://doi.org/10.1038/s41467-025-67548-0

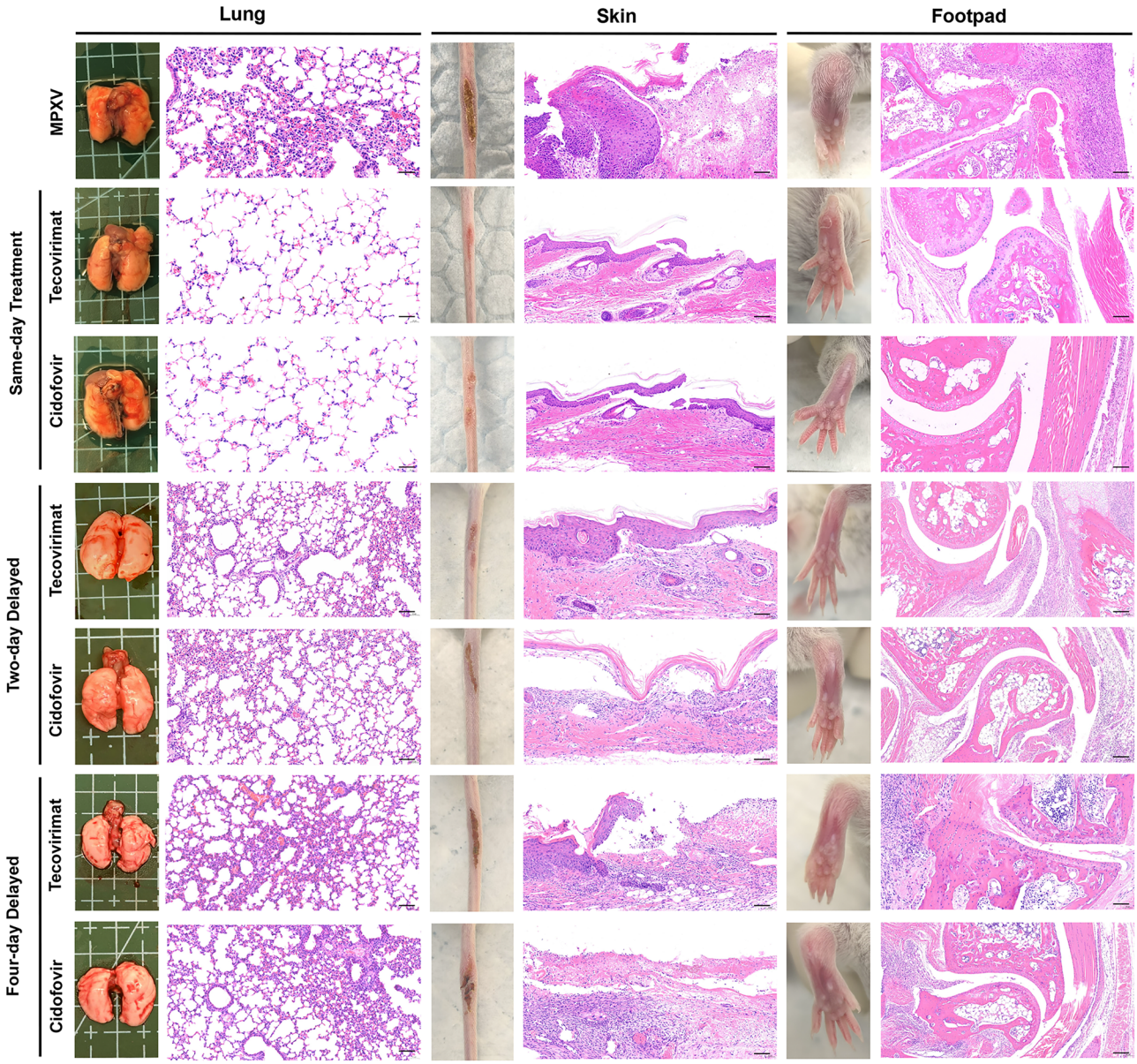

Fig. 5 | Clinical symptoms and histopathology sections of the lung, skin, and footpad. Clinical and histopathological changes in the lung, skin, and footpad were documented at 14 dpi in the models of pneumonia, rash, and local inflammation, respectively. The black scale bar in H&E figure represents 100 μm. The experiments were repeated independently eight times, and a representative result is shown for each.

persistently progressing disease. Therefore, we employed the same three SCID infection models used in early treatment but extended the treatment duration to 28 dpi to evaluate the therapeutic efficacy of tecovirimat and cidofovir in the late stage of MPXV infection (Fig. 6a). Both treatments effectively mitigated viral infection-induced weight loss (Fig. 6b–d). Both tecovirimat and cidofovir increased survival rates to 100% in the intranasal infection model (62.5% survival in the control group) and the subcutaneous infection model (0% survival in the control group) (Supplementary Fig. 5a–c). In the later stages of the disease, both drugs alleviated a range of clinical symptoms caused by viremia (Supplementary Fig. 5d–f).

Unfortunately, neither drug successfully inhibited scab formation at the scratch sites of the skin lesion model. In addition, the drugs did not reduce footpad swelling of the local inflammation model (Fig. 6e). Persistent viral presence in target organs may contribute to significantly elevated histopathological scores across all three models in treated animals. Histopathological scoring of the lung, skin, and footpad was performed according to established criteria detailed in Supplementary Tables 2–4. Notably, except for cidofovir, which significantly decreased the histopathological scores in the lung tissues of the pneumonia model (median = 6.5), no other treatment groups exhibited significant differences compared to the virus challenge groups (Fig. 6e, Supplementary Fig. 6a). In the intranasal infection model, tecovirimat and cidofovir significantly reduced viral loads and titers in the lungs and liver, with the downregulation in the lungs being significant. In contrast, suppression of DNA loads and viral titers in the spleen showed no statistically significant difference under these conditions (Fig. 6f). In the skin lesion model, neither drug significantly suppressed DNA loads and viral titers at the skin lesion. However, both drugs significantly reduced viral loads and titers in the lung and liver, and significantly reduced viral titers in the spleen (Fig. 6g). In the local inflammation model, tecovirimat and cidofovir significantly suppressed infectious viral titers at the footpad, lung, liver, and spleen. For the popliteal lymph nodes, no significant difference was observed in viral load, but a significant difference was found in viral titer (Fig. 6h). Significant differences in TNF-α and GM-CSF levels were observed

https://doi.org/10.1038/s41467-025-67548-0

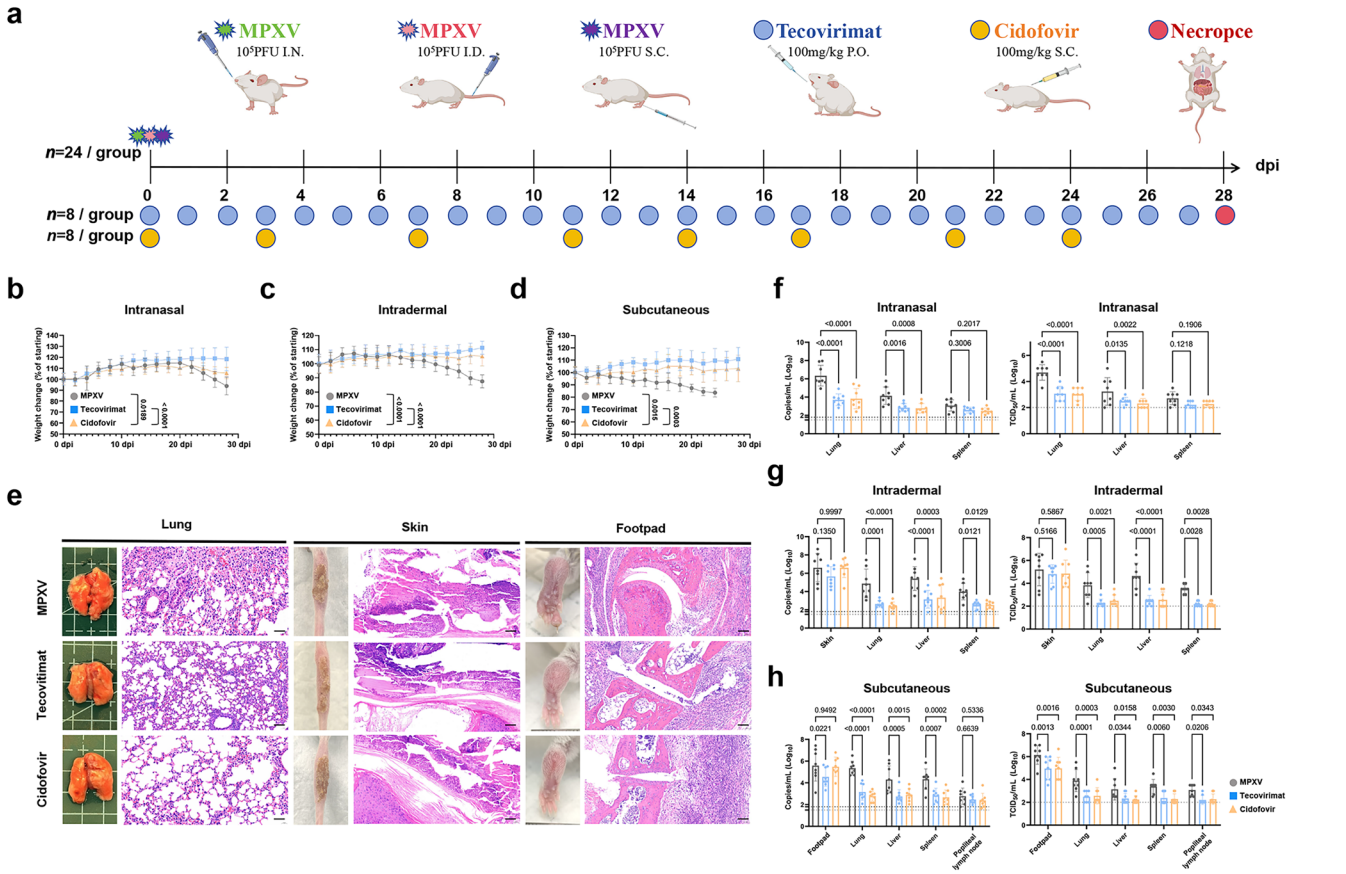

Fig. 6 | Therapeutic efficacy of tecovirimat and cidofovir in SCID mouse models of advanced MPXV clade IIb. a Study schematic of the in vivo evaluation of tecovirimat and cidofovir, use SCID mice with intranasal (green asterisk, n = 24), intradermal (pink asterisk, n = 24), and subcutaneous (purple asterisk, n = 24) infection routes. Tecovirimat (blue circle, P.O., n = 8), cidofovir (yellow circle, S.C., n = 8), or sterile saline (P.O. n = 4, S.C., n = 4) were administered for a 28-day treatment period. Surviving mice were euthanized (red) at 28 dpi, and those with a body weight loss exceeding 20% were euthanized earlier. Body weight changes were monitored across infection models: **b** intranasal, **c** intradermal, and **d** subcutaneous. **e** Clinical symptom assessments and histopathological observations were performed on the lung, skin, and footpad of the three disease models, respectively. The black scale bar in H&E figure represents 100 μm. Analysis of viral loads and titers in multiple organs demonstrated route-dependent efficacy: **f** intranasal, **g** intradermal, and **h** subcutaneous. Dashed line: limit of blank. Error bars represent the mean ± standard error of the mean (SEM). Statistical analysis was determined by one-way analysis of variance (ANOVA) followed by two-tailed *t*-tests. *P* values indicating statistical significance are displayed on the panels. Source data are provided as a Source data file. **a** was created with MedPeer (medpeer.cn).

between the treatment groups and the virus challenge group in the lung tissues of intranasal infection model. However, no changes were observed between the groups in the skin lesion model and the local inflammation model (Supplementary Fig. 6b).

In summary, in SCID mice with late-stage MPXV clade IIb infection, both tecovirimat and cidofovir effectively reduced mortality, maintained stable body weight, inhibited viral dissemination to secondary organs, and delayed the onset of skin lesions. However, neither drug prevented scab formation or footpad swelling in their respective infection models, and substantial viral loads were still detected in the primary target organs of the treated groups.

Discussion

Epidemiological data indicated that nearly half of patients with mpox suffer from HIV co-infection, which is associated with more severe clinical manifestations and higher mortality rates. A study conducted in the United States enrolled 395 patients with mpox, of whom 324 (82.0%) were diagnosed with HIV infection. In this cohort, severe mpox was observed in 19.5% of patients, and HIV co-infection was confirmed in 79.2% of patients[28]. However, clinical research on this population has been limited due to low healthcare-seeking rates and low availability of samples due to social stigma. While traditional non-human primate models (such as SIV-coinfected macaques) can simulate immunodeficiency phenotypes, their prohibitive maintenance costs and stringent ethical restrictions impede high-throughput research demands[29]. Therefore, rodent models have emerged as a favorable alternative.

Previous studies have demonstrated that 8-day-old neonatal ICR mice with their still-developing immune systems can experience transient MPXV clade IIb infection[30]. The 4–5-week ICR mice used in this study were resistant to MPXV clade IIb infection due to their fully functional immune systems. While IFNAR1$^{-/-}$ mice exhibit transient infection with MPXV clade IIb across all three infection models (intranasal, intradermal, and subcutaneous). Infectious viral particles peaked early during infection (3–7 dpi) in target organs but were largely cleared by day 14. Clinical signs such as scab at the tail and footpad swelling also gradually resolved. These findings indicate a mild, self-limiting infection course, partially consistent with prior studies of IFN-α/β receptor-deficient mice's low MPXV susceptibility[31]. It is well-established that SCID mice can be successfully infected with MPXV, as demonstrated in previous studies[32,33]. In this study, SCID mice were selected. Although CAST/EiJ mouse models of skin lesion and pulmonary infection models in BALB/c mice and dormice for clade IIb have been reported in recent years, these models only partly replicate localized symptoms or immune responses of MPXV-susceptible populations[27,34–36]. In contrast, SCID mice, characterized by congenital T/B lymphocyte developmental blockade due to Prkdc gene mutation, more accurately mimic the depletion of CD4$^+$ T cells observed in HIV-infected individuals[37]. Their persistent viral replication

and non-self-limiting disease progression closely align with the clinical manifestations of high-risk patients.

Tecovirimat and cidofovir, though not formally approved for mpox, are used in MPXV infections. Clinical practice often extends their course for severely immunocompromised patients[19,38–41]. This study, therefore, established an extended treatment group beyond the standard 14-day regimen. In the short-term model, we identify the administration windows for tecovirimat and cidofovir; however, they fail to prevent the virus from spreading from the target organ to local lymphoid tissues and systemic organs. When the disease progresses to the late stage, the treatment group can inhibit systemic infection but fail to suppress local symptoms. This limited therapeutic efficacy observed in advanced mpox aligns with a report from New York[42]. These findings indicate that for severely immunocompromised populations, antiviral therapy should be initiated early in disease progression, preferably supplemented with supportive therapies such as antiretroviral therapy (ART) and immunoglobulin infusion. When early cure is not achieved, and disease progresses to advanced stages, antiviral monotherapy generally insufficient, necessitating timely implementation of supportive measures, including complication management and local lesion treatment.

Clinically, pneumonia caused by mpox infection is predominantly observed among patients with HIV co-infection[8]. In patients with pneumonia, CT or X-ray examinations predominantly reveal pulmonary infiltration, ground-glass opacity, or consolidation, which are pathologically consistent with our pneumonia model[9,43]. Among all pathogenic models established in this study, the pneumonia model demonstrated the most favorable therapeutic outcomes, which can be attributed to the high blood flow in the lung and the high permeability of alveolar epithelium, facilitating drug accumulation in the lung tissues[44,45]. With the exception of a patient with acute respiratory distress syndrome (ARDS), where tecovirimat was successfully administered clinically, current management of patients with MPXV and confirmed pneumonia remains symptomatic treatment and supportive therapy, with no antiviral agents[46]. Given the favorable outcomes of both short-term and long-term treatments in this pneumonia model, it is suggested that tecovirimat and cidofovir can be considered to prevent severe adverse outcomes.

In the skin lesion model, tecovirimat demonstrated superior therapeutic efficacy compared to cidofovir. We speculate that this difference may be attributed to their distinct antiviral mechanisms and their respective activity and distribution profiles in skin tissue. MPXV infection via the skin requires progressive spread from the epidermis to the dermis, and tecovirimat inhibits further viral dissemination between skin tissues by blocking the VP37 protein. While cidofovir targets MPXV DNA polymerase during viral replication and theoretically also reduces production of infectious viral particles, it appears less effective than tecovirimat in preventing the expansion of skin lesions and development of severe tissue damage. Some drugs may have limited tissue distribution in highly keratinized skin[47–49]. Currently, there are reports of the topical application or injection of cidofovir for the treatment of Poxviridae viruses[23,50]. Compared with systemic administration, local drug delivery increases its distribution in skin tissues, serving as a potential method to enhance the therapeutic efficacy of cidofovir for rashes. Although cidofovir did not reduce the viral load in the skin of the intradermal infection model, it unexpectedly lowered the viral load in the lung tissue of SCID mice. This finding is consistent with the therapeutic effects of cidofovir on skin infections caused by cowpox virus[50].

In the local infection model, according to previous relevant reports[51,52], popliteal lymph node served as a key site distinguishing localized from systemic infection. We confirmed that MPXV clade IIb spreads from the footpad through the popliteal lymph node to the lung, liver, and spleen. MPXV dissemination from the lymph node to visceral organs induced secondary viremia, leading to secondary rash in untreated groups. Notably, although viral loads remained detectable in the visceral organs of the long-term treatment group, no secondary rash was observed, indicating that both tecovirimat and cidofovir can delay the onset of secondary viremia. Furthermore, based on the clinical manifestations of local infection, we demonstrated for the first time in vitro that muscle cells and osteoblasts are susceptible to MPXV clade IIb infection. Both tecovirimat and cidofovir exhibited potent antiviral efficacy in these cellular models.

In summary, this study successfully established a SCID mouse infection model of MPXV clade IIb, characterized by pneumonia, lesions, and localized inflammation. All models developed extensive systemic infection and secondary rashes in the advanced stage of the disease. Based on the aforementioned models, our findings revealed that the timing of treatment initiation and the stage of disease progression exert a critical impact on the anti-MPXV efficacy of tecovirimat and cidofovir. These results highlight the important clinical significance of early intervention during the therapeutic window for immunocompromised mpox patients, and suggest that monotherapy may be difficult to achieve optimal therapeutic effects in the advanced stage of the disease. Therefore, clinical management strategies should consider combining appropriate supportive care measures with antiviral treatment to optimize treatment outcomes.

Methods

Cells and virus

The MPXV strain (clade IIb, GenBank number: PP778666.1) was donated by the Eighth Affiliated Hospital of Guangzhou Medical University. The isolation procedure was approved by the Ethics Committee of Guangzhou Eighth People's Hospital, Guangzhou Medical University (Approval No.: 202311248). All participants provided written informed consent, which was the review procedure of the ethics committee. The virus was cultured and amplified in Vero-E6 cells using DMEM medium (Sigma-Aldrich) containing 2% fetal bovine serum (FBS), 50 U/mL penicillin, and 50 μg/mL streptomycin. This study utilized five cell lines: A549 (human non-small cell lung carcinoma, Procell Cat# CL-0016, male origin), HaCaT (human immortalized keratinocytes, Procell Cat# CL-0090, male origin), LHCN-M2 (human myoblasts, Procell Cat# CL-0667, male origin), MC3T3 (mouse pre-osteoblasts, Procell Cat# CL-0161, sex not applicable), and Vero-E6 (African green monkey kidney cells, Procell Cat# CL-0169, sex not applicable). A549, HaCaT, MC3T3, and Vero-E6 cells were cultured in DMEM supplemented with 10% FBS, 50 U/mL penicillin, and 50 μg/mL streptomycin. LHCN-M2 cells were cultured in a specialized medium consisting of a 4:1 mixture of DMEM (high glucose) and Medium 199, further supplemented with 15% FBS, 200 mM HEPES, 0.03 μg/ml zinc sulfate, 1.4 μg/ml vitamin B12, 0.055 μg/ml dexamethasone, 2.5 ng/ml hepatocyte growth factor, 10 ng/ml basic fibroblast growth factor, 50 U/mL penicillin, and 50 μg/mL streptomycin. No mycoplasma or contaminants were detected. All human-derived cell lines (A549, HaCaT, and LHCN-M2) were authenticated using short tandem repeat (STR) profiling. Non-human cell lines (MC3T3 and Vero-E6) were authenticated by species-specific PCR. All experiments involving infectious MPXV were conducted in a biosafety level 3 laboratory.

Animal experiment design

Four-to-five-week-old male ICR mice (outbred, *Mus musculus*), SCID mice (NOD.CB17-Prkdc scid/NcrCrl, *Mus musculus*), and IFNAR1$^{-/-}$ mice (C57BL/6J background, *Mus musculus*) were obtained from Beijing HFK Biotechnology Co., Ltd. (ICR mice, Catalog No.: 1101; SCID mice, Catalog No.: 1401) and Beijing Cyagen Biosciences Inc. (IFNAR1$^{-/-}$ mice, Catalog No.: C001458). This study utilized only male animals. All mice were anesthetized with isoflurane and inoculated via intranasal, intradermal (tail), and subcutaneous (footpad) routes with either MPXV clade IIb (10^5 PFU) or normal saline. Part 1: ICR, IFNAR1$^{-/-}$, and SCID mice (n = 24 MPXV clade IIb infected; n = 8 saline per model) were

monitored for clinical symptoms and euthanized at 3, 7, and 14 dpi, respectively. Part 2: SCID mice (n = 24 MPXV clade IIb infected; n = 8 saline) were used for disease scoring and survival assessment from 0 to 28 dpi. Part 3: MPXV clade IIb-infected SCID mice (n = 80) were treated with tecovirimat (oral, 100 mg/kg, daily; n = 16), cidofovir (subcutaneous, 100 mg/kg, twice weekly; n = 32), or normal saline (oral and subcutaneous controls; n = 32). Treatment regimens included initiation on the day of infection (same-day treatment), a short-term extension for 2 days, or a delayed start by 4 days. Mice were euthanized at 14 and 28 dpi (n = 8 per group per time point). All animals in this study were euthanized at the experimental endpoint in accordance with animal ethical welfare regulations and the guidelines of the AVMA Guidelines for the Euthanasia of Animals. Tissues including lung, skin, footpad, liver, spleen, and popliteal lymph nodes were collected, minced, weighed to 0.1 g (wet weight), and homogenized in 500 μL PBS for subsequent analysis.

All experimental mice were housed in a specific pathogen-free barrier environment under a 12-h light/12-h dark cycle, with ambient temperature maintained at 22 ± 1 °C and relative humidity kept at 50% ± 10%. The mice were housed eight per cage with sterile bedding and had ad libitum access to sterile standard diet and filtered drinking water. These housing conditions remained constant throughout the experimental period and fully complied with the Association for Assessment and Accreditation of Laboratory Animal Care International guidelines.

In vitro antiviral efficacy assays

CC_{50} Determination: Vero-E6 cell monolayers in 96-well plates were cultured to approximately 50% confluence and treated with different concentrations of tecovirimat (200, 40, 8, 1.6, 0.32, 0.064, 0.0128, and 0.00256 μM) or cidofovir (200, 40, 8, 1.6, 0.32, 0.064, 0.0128, and 0.00256 μM) in a total volume of 100 μL per well. Each drug concentration was prepared by five-fold serial dilution in the maintenance medium. After 72 h of incubation, the medium was discarded, and the cells were washed twice with PBS. Subsequently, 100 μL of 10% CCK-8 reagent was added to each well, followed by incubation in a 5% CO_2 incubator at 37 °C for 0.5–1 h. The absorbance (OD) was measured at 450 nm using a microplate reader.

EC_{50} Determination: Vero-E6 cells were cultured in 24-well plates to near confluence and infected with MPXV clade IIb at an MOI of 0.1. The infection was incubated for 1 h at 37 °C with 5% CO_2, shaking every 15 min. After removing the inoculum, different concentrations of tecovirimat or cidofovir were added based on CC_{50}. After a 72-h incubation period, the supernatants were collected, and MPXV DNA was extracted using the MAGEN DNA extraction kit. The viral DNA levels were quantified by qPCR. The OD values and corresponding DNA copy numbers were entered into GraphPad Prism software, normalized to the control group (cells treated with no drug), and expressed as percentages. The concentrations (log-transformed) were plotted on the X-axis, and the percentage of cell viability or MPXV DNA content was plotted on the Y-axis. A four-parameter logistic curve was fitted, and nonlinear regression analysis was conducted to calculate the CC_{50} and EC_{50} values for each treatment group.

Viral DNA quantification (qRT-PCR)

Tissue homogenates were centrifuged at 12,000 × *g* and 4 °C for 15 min, and the supernatant (200 μL) was collected to detect and quantify the expression levels of MPXV. Viral nucleic acid was extracted using the Viral Nucleic Acid Quick Extraction Kit (MAGEN) following the manufacturer's instructions, with an elution volume of 50 μL. Real-time fluorescence quantitative detection of the MPXV F3L gene was conducted using the TaqMan probe method (F: 5′-CTCATTGATTTTTCGCGGGATA-3′, R: 5′-GACGATACTCCTCCTCGTTGGT-3′, probe: FAM-CATCAGAATCTGTAGGCCGT-BHQ). The experiment was conducted using the Takara Premix Ex Taq™ (Probe qPCR) kit (TAKARA) for Real-Time PCR. The experiment was conducted using the Takara Premix Ex Taq™ (Probe qPCR) kit (TAKARA) for Real-Time PCR. The reactions were conducted on the Bio-Rad CFX96 Real-Time PCR Detection System. All primers and probes were synthesized by Sangon Biotech (Shanghai) Co., Ltd.

Infectious virus titer quantification ($TCID_{50}$)

The supernatant of tissue homogenate was serially diluted 10-fold. Then, 100 μL of each dilution was added to a 96-well plate containing a monolayer of Vero-E6 cells. The plate was incubated in a 5% CO_2 at 37 °C. After 96 h of incubation, the cytopathic effect (CPE) was observed. The virus titer was calculated using the Reed-Muench method.

Histopathological assessment

Necropsy and tissue sampling were conducted following the protocols approved by the Institutional Biosafety Committee (IBC). Hematoxylin and eosin (H&E) staining of tissue samples was conducted using standard paraffin embedding methods. Tissue samples were fixed in 10% neutral-buffered formalin for at least 7 days, followed by dehydration, clearing, and embedding in paraffin. The tissues were sectioned into 4–5 μm thick slices and mounted onto pre-coated APES slides. The tissue slides were deparaffinized in xylene, rehydrated through ethanol, stained with hematoxylin and eosin, and dehydrated. After clearing in xylene, the tissue sections were mounted with neutral balsam. The tissue slides were evaluated by a certified, double-blind pathologist.

Measurement of cytokine levels

RNA was extracted from 200 μL of homogenized tissue using an RNA Extraction Kit (Gene Script Biotech). The extracted mRNA was amplified in a CFX96 Real-Time PCR System (Bio-Rad) using the commercially available 2× Q1 SYBR qPCR Master Mix (Universal). For cytokine profiling, the following primer pairs were used: *TNF-α* (F: 5′-AGCCAGGAGGGAGAACAGA-3′, R: 5′-CAGTGAGTGAAAGGGACAGAAC-3′), *IL-6* (F: 5′-CGGAGAGGAGACTTCACAGAG-3′, R: 5′-CATTTCCACGATTTCCCAGA-3′), *NAP3* (F: 5′-TCCAGAGCTTGAAGGTGTTGCC-3′, R: 5′-AACCAAGGGAGCTTCAGGGTCA-3′), *IFN-α1* (F: 5′-TAATTCCTACGTCTTTTCTTT-3′, R: 5′-TATGCCTGATCCCTGAACAGT-3′), *IFN-β* (F: 5′-AACCTCCTGGATGACATGCCTG-3′, R: 5′-AAATTGCCCCGTAGACCCTGCT-3′), *GM-CSF* (F: 5′-AACCTCCTGGATGACATGCCTG-3′, R: 5′-AAATTGCCCCGTAGACCCTGCT-3′) Expression levels were normalized to *β-actin* (F: 5′-GTGGGCCGCTCTAGGCACCAA-3′, R: 5′-CTCTTTGATGTCACGCACGATTTC-3′). The 2× Q1 SYBR qPCR Master Mix (Universal) was employed for qPCR.

Cytokine levels were measured using the TNF-α ELISA Kit and GM-CSF ELISA Kit (Cloud-Clone Corp.). The homogenate was centrifugated and lysed with RIPA buffer to prepare for inflammatory factor detection. The experiments were conducted following the manufacturer's instructions, and the absorbance was read at 450 nm using a spectrophotometer.

Statistical analysis and data visualization

Data collection and analysis were conducted in a double-blind manner. The HE staining experiments were independently repeated eight times, and one representative result image was shown for each group. $TCID_{50}$, qPCR, and ELISA analyses were performed once, with eight replicates per sample. Statistical analyses were conducted using GraphPad Prism 8.0. Data are presented as mean ± standard error of the mean (SEM). Inter-group differences were determined using *t*-tests or one-way analysis of variance (ANOVA) followed by two-tailed *t*-tests, unless otherwise specified. *P* values indicating statistical significance are displayed on the panels. The type of test used is indicated where appropriate. All data generated in this study are provided in the Source data file.

Ethics statement

All animal experiments were conducted in AAALAC International-accredited facilities and adhered to the National Institutes of Health (NIH) Guide for the Care and Use of Laboratory Animals. The experiments were approved by the Animal Care and Use Committee of the Changchun Veterinary Research Institute (IACUC approval no. AMMS-11-2023-041). All samples generated in the biosafety level 3 laboratory were inactivated according to IBC-approved standard operating procedures upon removal from the high-containment area.

Reporting summary

Further information on research design is available in the Nature Portfolio Reporting Summary linked to this article.

Data availability

The source data generated in this study are provided in the Supplementary Information file. The source data used in this study are also available in the Figshare repository under accession code https://doi.org/10.6084/m9.figshare.28827320. No third-party or publicly available datasets were utilized. Source data are provided with this paper.

References

1. Jezek, Z., Szczeniowski, M., Paluku, K. M. & Mutombo, M. Human monkeypox: clinical features of 282 patients. *J. Infect. Dis.* **156**, 293–298 (1987).
2. Isidro, J. et al. Phylogenomic characterization and signs of microevolution in the 2022 multi-country outbreak of monkeypox virus. *Nat. Med.* **28**, 1569–1572 (2022).
3. Gigante, C. M. et al. Multiple lineages of monkeypox virus detected in the United States, 2021-2022. *Science* **378**, 560–565 (2022).
4. Patiño, L. H. et al. Phylogenetic landscape of Monkeypox Virus (MPV) during the early outbreak in New York City, 2022. *Emerg. Microbes Infect.* **12**, e2192830 (2023).
5. Bunge, E. M. et al. The changing epidemiology of human monkeypox-A potential threat? A systematic review. *PLoS Negl. Trop. Dis.* **16**, e0010141 (2022).
6. Desingu, P. A., Rubeni, T. P. & Sundaresan, N. R. Evolution of monkeypox virus from 2017 to 2022: In the light of point mutations. *Front. Microbiol.* **13**, 1037598 (2022).
7. Laurenson-Schafer, H. et al. Description of the first global outbreak of mpox: an analysis of global surveillance data. *Lancet Glob. Health* **11**, e1012–e1023 (2023).
8. Mitjà, O. et al. Mpox in people with advanced HIV infection: a global case series. *Lancet* **401**, 939–949 (2023).
9. Sun, G. et al. The first human to have necrotizing pneumonia secondary to monkeypox infection. *Chest* **164**, A1325–A1326 (2023).
10. Thornhill, J. P. et al. Monkeypox virus infection in humans across 16 countries—April-June 2022. *N. Engl. J. Med.* **387**, 679–691 (2022).
11. O'Shea, J. et al. Prolonged mpox disease in people with advanced HIV: characterization of mpox skin lesions. *J. Infect. Dis.* **229**, S243–s8 (2024).
12. Lombès, A. et al. Arthritis due to monkeypox virus: a case report. *Jt. Bone Spine* **90**, 105492 (2023).
13. Fonti, M. et al. Monkeypox associated acute arthritis. *Lancet Rheumatol.* **4**, e804 (2022).
14. Mungmunpuntipantip, R. & Wiwanitkit, V. Comment on "Arthritis due to monkeypox virus: a case report" by Lombès A et al. Joint Bone Spine. 2023;90:105492. *Jt. Bone Spine* **90**, 105518 (2023).
15. Paparini, S. et al. "If that would have lessened my symptoms, that would have been great…": a qualitative study about the acceptability of tecovirimat as treatment for mpox. *BMC Med.* **23**, 19 (2025).
16. Shabil, M. et al. Effectiveness of tecovirimat in mpox cases: a systematic review of current evidence. *J. Med. Virol.* **96**, e70122 (2024).
17. Shannon, A. & Canard, B. Nucleotide analogues and mpox: repurposing the repurposable. *Antivir. Res.* **234**, 106057 (2025).
18. Yu, P. A., Elmor, R., Muhammad, K., Yu, Y. C. & Rao, A. K. Tecovirimat use under expanded access to treat mpox in the United States, 2022-2023. *NEJM Evid.* **3**, EVIDoa2400189 (2024).
19. Fortier, J. C., Marsalisi, C., Cordova, E., Guo, H. J. & Verdecia, J. Challenges in managing treatment-resistant mpox complicated by severe superinfection. *Open Forum Infect. Dis.* **11**, ofae138 (2024).
20. Smith, T. G. et al. Tecovirimat resistance in mpox patients, United States, 2022-2023. *Emerg. Infect. Dis.* **29**, 2426–2432 (2023).
21. Lenharo, M. Hopes dashed for drug aimed at monkeypox virus spreading in Africa. *Nature* **632**, 965 (2024).
22. Gigante, C. M. et al. Notes from the field: mpox cluster caused by tecovirimat-resistant monkeypox virus—five states, October 2023-February 2024. *MMWR Morb. Mortal. Wkly. Rep.* **73**, 903–905 (2024).
23. Stafford, A. et al. Use of cidofovir in a patient with severe mpox and uncontrolled HIV infection. *Lancet Infect. Dis.* **23**, e218–e226 (2023).
24. Cundy, K. C. et al. Clinical pharmacokinetics of cidofovir in human immunodeficiency virus-infected patients. *Antimicrob. Agents Chemother.* **39**, 1247–1252 (1995).
25. Sobral-Costas, T. G. et al. Human monkeypox outbreak: epidemiological data and therapeutic potential of topical cidofovir in a prospective cohort study. *J. Am. Acad. Dermatol.* **88**, 1074–1082 (2023).
26. Prévost, J. et al. Treatment efficacy of cidofovir and brincidofovir against clade II Monkeypox virus isolates. *Antivir. Res.* **231**, 105995 (2024).
27. Cheng, L. et al. Pathogenic BALB/c mice infection model for evaluation of mpox countermeasures. *Cell Discov.* **10**, 105 (2024).
28. Aldred, B. et al. Associations between HIV and severe mpox in an Atlanta Cohort. *J. Infect. Dis.* **229**, S234–S242 (2023).
29. Li, Q. et al. Glycerol monolaurate prevents mucosal SIV transmission. *Nature* **458**, 1034–1038 (2009).
30. Sergeev, A. A. et al. The possibility of using the ICR mouse as an animal model to assess antimonkeypox drug efficacy. *Transbound. Emerg. Dis.* **63**, e419–e430 (2016).
31. Wei, Z. K. et al. Animal models of mpox virus infection and disease. *Infect. Med.* **2**, 153–166 (2023).
32. Osorio, J. E., Iams, K. P., Meteyer, C. U. & Rocke, T. E. Comparison of monkeypox viruses pathogenesis in mice by in vivo imaging. *PLoS ONE* **4**, e6592 (2009).
33. Wang, X. et al. Differential susceptibility of immunodeficient mice to MPXV infection and the impact of various inoculation routes. *Virol. Sin.* **40**, 333–339 (2025).
34. Song, G. et al. Establishment of an animal model for monkeypox virus infection in dormice. *Sci. Rep.* **15**, 4044 (2025).
35. Warner, B. M. et al. In vitro and in vivo efficacy of tecovirimat against a recently emerged 2022 monkeypox virus isolate. *Sci. Transl. Med.* **14**, eade7646 (2022).
36. Meyer Zu Natrup, C. et al. Strong and early monkeypox virus-specific immunity associated with mild disease after intradermal clade-IIb-infection in CAST/EiJ-mice. *Nat. Commun.* **16**, 1729 (2025).
37. Nonoyama, S. & Ochs, H. D. Immune deficiency in SCID mice. *Int. Rev. Immunol.* **13**, 289–300 (1996).
38. Duong, M. T. et al. Combination of extended antivirals with antiretrovirals for severe mpox in advanced human immunodeficiency virus infection: case series of 4 patients. *Open Forum Infect. Dis.* **11**, ofae110 (2024).
39. Siegrist, E. A. & Sassine, J. Antivirals with activity against mpox: a clinically oriented review. *Clin. Infect. Dis.* **76**, 155–164 (2023).
40. De Clercq, E. Cidofovir in the treatment of poxvirus infections. *Antivir. Res.* **55**, 1–13 (2002).
41. Bourner, J. et al. Expanded Access Programme for the use of tecovirimat for the treatment of monkeypox infection: a study

protocol for an Expanded Access Programme. *PLoS ONE* **19**, e0278957 (2024).
42. Garcia, E. A. et al. Severe mpox among people with advanced human immunodeficiency virus receiving prolonged tecovirimat in New York City. *Open Forum Infect. Dis.* **11**, ofae294 (2024).
43. Ciepłucha, H. D., Bożejko, M., Piesiak, P., Serafińska, S. & Szetela, B. Bacterial pneumonia and cryptogenic pleuritis after probable monkeypox virus infection: a case report. *Infect. Dis. Rep.* **15**, 795–805 (2023).
44. Alrashedi, M. G., Ali, A. S., Ahmed, O. A. & Ibrahim, I. M. Local delivery of azithromycin nanoformulation attenuated acute lung injury in mice. *Molecules* **27**, 8293 (2022).
45. Smola, M., Vandamme, T. & Sokolowski, A. Nanocarriers as pulmonary drug delivery systems to treat and to diagnose respiratory and non respiratory diseases. *Int. J. Nanomed.* **3**, 1–19 (2008).
46. Tchoubou, T. et al. Acute respiratory distress syndrome due to monkeypox virus. *Eur. J. Case Rep. Intern. Med.* **10**, 004126 (2023).
47. Bagley, D. H., Mac Lowry, J., Beazley, R. M., Gorschboth, C. & Ketcham, A. S. Antibiotic concentration in human wound fluid after intravenous administration. *Ann. Surg.* **188**, 202–208 (1978).
48. Prausnitz, M. R. & Langer, R. Transdermal drug delivery. *Nat. Biotechnol.* **26**, 1261–1268 (2008).
49. Yang, Y. et al. Recent advances in oral and transdermal protein delivery systems. *Angew. Chem.* **62**, e202214795 (2023).
50. Tarbet, E. B. et al. Evaluation of imiquimod for topical treatment of vaccinia virus cutaneous infections in immunosuppressed hairless mice. *Antivir. Res.* **90**, 126–133 (2011).
51. Stabenow, J. et al. A mouse model of lethal infection for evaluating prophylactics and therapeutics against Monkeypox virus. *J. Virol.* **84**, 3909–3920 (2010).
52. Parker, S., Siddiqui, A. M., Painter, G., Schriewer, J. & Buller, R. M. Ectromelia virus infections of mice as a model to support the licensure of anti-orthopoxvirus therapeutics. *Viruses* **2**, 1918–1932 (2010).

Acknowledgements

This work was supported by the National Key Research and Development Program of China (2023YFD1800405) and CAMS Innovation Fund for Medical Sciences (2020-12M-5-001). Thanks to the Eighth Affiliated Hospital of Guangzhou Medical University for donating the MPXV strain. The authors would like to express their gratitude to Edit Springs (https://www.editsprings.cn) for the expert linguistic services provided.

Author contributions

X.Y.C., N.S., X.L., Y.B.X., Y.L.S., and H.J.L. designed the research. X.Y.C., X.S.Q., J.X.T., P.W., B.C.L., Z.H., H.Z., C.S., and X.L. performed the research. All authors analyzed and interpreted the data. X.Y.C. wrote the paper.

Competing interests

The authors declare no competing interests.

Additional information

Supplementary information The online version contains supplementary material available at https://doi.org/10.1038/s41467-025-67548-0.

Correspondence and requests for materials should be addressed to Yubiao Xie, Yuelong Shu or Huijun Lu.

Peer review information *Nature Communications* thanks Zheng Zhang and the other, anonymous, reviewer(s) for their contribution to the peer review of this work. A peer review file is available.